

Golden Partition Zone: Rethinking Neural Network Partitioning Under Inversion Threats in Collaborative Inference

Rongke Liu

Nanjing University of Aeronautics and Astronautics
Nanjing, Jiangsu, China
liurongke@nuaa.edu.cn

Youwen Zhu

Nanjing University of Aeronautics and Astronautics
Nanjing, Jiangsu, China

ABSTRACT

In collaborative inference, intermediate features transmitted from edge devices can be exploited by adversaries to reconstruct original inputs via model inversion attacks (MIA). While existing defenses focus on shallow-layer protection, they often incur significant utility loss. A key open question is how to partition the edge-cloud model to maximize resistance to MIA while minimizing accuracy degradation. We first overturn the common belief that increasing model depth can resist MIA. Through theoretical analysis, we show that representational transitions in neural networks cause sharp changes in conditional entropy $H(x|z)$, intra-class mean-squared radius R_c^2 and feature dimensionality being critical factors. Experiments on three representative deep vision models show that partitioning at the representational transition or decision-level layers yields over $4\times$ higher mean square error compared to shallow splits, indicating significantly stronger resistance to MIA. Positive label smoothing further enhances robustness by compressing R_c^2 and improving generalization. We also validate the resilience of decision-level features under feature and inversion model enhancements, and observe that auxiliary data types influence both transition boundaries and reconstruction behavior.

CCS CONCEPTS

• **Security and privacy** → **Domain-specific security and privacy architectures.**

KEYWORDS

Model inversion attack, Collaborative inference, Information entropy

ACM Reference Format:

Rongke Liu and Youwen Zhu. 2018. Golden Partition Zone: Rethinking Neural Network Partitioning Under Inversion Threats in Collaborative Inference. In *Proceedings of Proceedings of the ACM Web Conference 2026* ((www '26). ACM, New York, NY, USA, 12 pages. <https://doi.org/XXXXXXX.XXXXXXX>

Permission to make digital or hard copies of all or part of this work for personal or classroom use is granted without fee provided that copies are not made or distributed for profit or commercial advantage and that copies bear this notice and the full citation on the first page. Copyrights for components of this work owned by others than the author(s) must be honored. Abstracting with credit is permitted. To copy otherwise, or republish, to post on servers or to redistribute to lists, requires prior specific permission and/or a fee. Request permissions from permissions@acm.org.

(www '26, June 03–05, 2018, Woodstock, NY)

© 2018 Copyright held by the owner/author(s). Publication rights licensed to ACM.

ACM ISBN 978-1-4503-XXXX-X/2018/06...\$15.00

<https://doi.org/XXXXXXX.XXXXXXX>

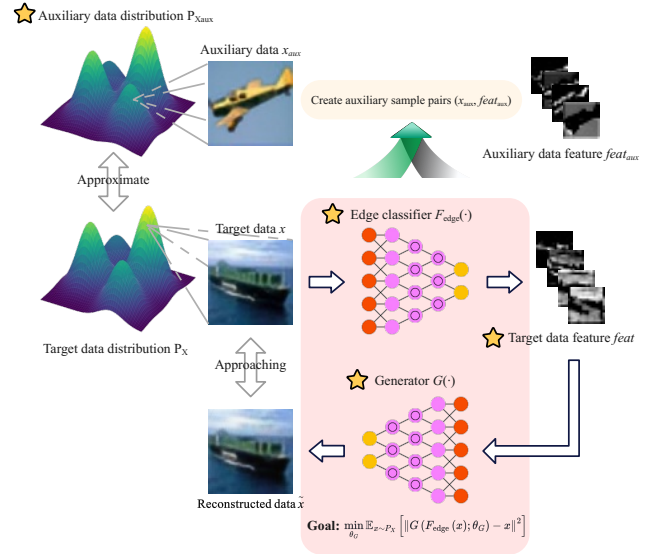


Figure 1: Paradigm of MIA under collaborative inference, with ★ indicating the parts covered in this work.

1 INTRODUCTION

Collaborative inference (CI) has become a widely adopted paradigm in edge-cloud computing, where a deep neural network is partitioned between an edge device and a cloud server. This design enables efficient inference by allowing the edge to perform early computations while the cloud processes the remaining layers. The method supports real-time performance and has seen broad adoption in UAVs [27], IoT systems [29], and private cloud computing (PCC) [12]. With the continued rise of 5G, IoT, and AI, CI is expected to become even more prevalent. However, the intermediate features transmitted from the edge to the cloud expose new privacy risks. Recent studies have shown that these features can be exploited by adversaries to reconstruct the original input through model inversion attacks (MIA).

As illustrated in Fig. 1, MIA under collaborative inference aims to train a generator using auxiliary data that approximates the target distribution, such that the generator can approximate the inverse mapping of the edge-side model. Unlike centralized MIA [21, 38], which typically reconstructs class-level distributions, collaborative inference's MIA [2, 16] focuses on reconstructing individual samples, making it a more fine-grained and privacy-critical threat.

Most existing works on MIA, both attacks and defenses, have not systematically explored deep vision models and typically focus only on shallow layers. Defense strategies can be broadly categorized into follow types: adding noise [34], applying masks [9], increasing

model depth, or using information-theoretic estimators to induce bottlenecks [11, 35]. While these methods can theoretically suppress input reconstruction, they often come at the cost of reduced model utility and degraded generalization. More fundamentally, they overlook a key question: *Where should we partition the model to achieve the strongest resistance to MIA with minimal impact on accuracy?* Identifying such a zone could enable more effective and diverse defense strategies in the future.

In this work, we first challenge the common intuition that increasing model depth can resist MIA. Our experiments reveal that increasing depth alone does not ensure protection; instead, effective resistance requires the mutual information $I(x, z)$ between the input x and intermediate information z to drop sufficiently to suppress inversion. From an information-theoretic perspective, we derive a lower bound on the conditional entropy $H(x|z)$, and show that it undergoes a sharp increase when the representation shifts from feature-level to decision-level. Within this representational transition zone and beyond, we identify two key factors that dominate $H(x|z)$: feature dimensionality D and intra-class mean-squared radius (R_c^2). By adjusting these factors, one can effectively raise $H(x|z)$ and reduce the success of MIA.

Based on these insights, we conduct experiments on three representative deep vision models, IR-152 [15], VGG19 [30], and ViT [10], and demonstrate that partitioning at the representational transition or decision-level layers leads to significantly improved resistance to MIA. In addition, we introduce targeted enhancement strategies for both features and inversion model design, revealing that even standard MIA pipelines have room for improvement. Specifically, we propose mathematically grounded and neural network-based techniques to enrich the transmitted features, and incorporate a progressive attention mechanism, from weakly to strongly decoupled, to better approximate the behavior of $H(x|z)$. Experiments confirm that decision-level representations exhibit 66% stronger resistance on average compared to feature-level representations.

Finally, we explore how data characteristics influence representational transitions and reconstruction quality. We find that increasing the number of classes shifts the transition boundary earlier in the network, and that data types with greater intra-class diversity tend to yield higher resistance to inversion.

Our main contributions are summarized as follows:

- We overturn the common belief that increasing model depth can resist MIA, and identify a sharp increase in $H(x|z)$ after the representational transition, along with the influence of intra-class mean-squared radius and feature dimensionality on its lower bound.
- We validate on three representative deep vision models that the representational transition zone and the decision-level region offer strong resistance to MIA.
- We apply targeted enhancements to both transmitted features and inversion models, further verifying the superior resistance of decision-level representations compared to feature-level ones.
- We examine how different data types affect the location of the representational transition and the final reconstruction quality.

2 THREAT MODEL

This work adopts a standard threat model widely used in vision-based inversion research and focuses on image and visual models.

2.1 Collaborative Inference Setting

In collaborative inference (CI), the information flow typically follows a pipeline of the form $x \xrightarrow{f_{\text{edge}}} z \xrightarrow{f_{\text{cloud}}} y$, where the deep model is split into an edge-side component f_{edge} and a cloud-side component f_{cloud} . The edge device is typically controlled by the end user, who owns and supplies the sensitive input x . This edge component performs early-layer computations and transmits intermediate features z to the cloud. The cloud server, managed by a service provider or platform administrator, completes the remaining computation and returns the final prediction y , either for direct feedback or further downstream processing.

In this setup, the cloud may either act as the adversary or be compromised by one. Alternatively, the attacker may eavesdrop on the transmission of intermediate features. However, the adversary does not have access to the raw input x .

It is crucial to emphasize that even if the attacker does not reside on the cloud and secure transmission protocols such as TLS (Transport Layer Security) [8] are employed, privacy risks remain fundamentally unresolved. These protocols may prevent plaintext leakage during transmission, but they offer no protection against the semantic content inherently embedded in the intermediate features z . These features often retain rich and structured information from the original input x , making them highly vulnerable to inversion-based reconstruction. In other words, the threat is not merely in how the data is transmitted, but in what is being transmitted. Without addressing the information content of z , transport-layer encryption alone is insufficient to guarantee privacy in collaborative inference systems.

2.2 Model Inversion Attack

The goal of the adversary is to reconstruct the original input x from the intermediate feature z , by learning an approximate inverse mapping $g \approx f_{\text{edge}}^{-1}$. This attack can be carried out in both white-box and black-box settings. The specific attack strategy considered in this work follows the standard pipeline described in Section 4.1.

3 THEORETICAL ANALYSIS FOR MODEL PARTITIONING

This section establishes a theoretical framework elucidating how the transition from feature-level to decision-level representations enhances resistance to MIAs. We begin by fixing the notation. Then, we challenge the prevailing intuition that deeper model partitions inherently strengthen defenses against MIAs, instead identifying the representational transition zone as the critical locus of inversion resistance. Next, we rigorously derive the connection between class-wise mean-squared radius and conditional entropy, highlighting its implications for model robustness. Finally, we critically evaluate label smoothing's dual role in contracting decision-region radii and modulating inversion-attack vulnerability.

Table 1 summarizes fundamental symbols and expressions used throughout derivations, ensuring clarity and unambiguous reference in subsequent analyses.

Table 1: Notation used in the theoretical analysis.

Symbol	Definition
K, c	Number of classes & Class index
$z_i \in \mathbb{R}^{d_\ell}$	Feature of sample i at layer ℓ
$Z = (z^{(1)}, \dots, z^{(B)}) \in \mathbb{R}^{Bd}$	Batch concatenation of B feature vectors
$\mu_c = \frac{1}{N_c} \sum_{i \in c} z_i$	Class center
$\Sigma_c = \frac{1}{N_c} \sum_{i \in c} (z_i - \mu_c)(z_i - \mu_c)^\top$	Class covariance
$o_i = f_{\text{cloud}}(z_i) \in \mathbb{R}^K, p_i = \text{softmax}(o_i)$	Sample logits and predicted probabilities
$J_i = \frac{\partial o_i}{\partial z_i}$	Jacobian of logits w.r.t. features
e_c, e_k	unit vector for c and k -th unit vector in \mathbb{R}^K
$\delta = \frac{\partial \mathcal{L}_{\text{CE}}}{\partial o_i} = p_i - y_i$	CE gradient w.r.t. logits
$\tilde{\delta} = \frac{\partial \mathcal{L}_{\text{LS}}}{\partial o_i} = p_i - y'_i$	LS gradient ($y'_c = 1 - \alpha, y'_k = \alpha/K$)

3.1 Representational Transition Zone

The mutual information between the input x and an intermediate representation z is defined as:

$$I(x, z) = H(x) - H(x|z) = H(z) - H(z|x) \quad (1)$$

When the mapping $F_{\text{edge}} : x \mapsto z$ is deterministic, as in standard feedforward networks [35], $H(z|x) = 0$, and thus $I(x, z) = H(z)$.

In standard feedforward networks, feature transformations form a Markov chain, and by the data processing inequality:

$$I(x, z_{\ell 1}) \geq I(x, z_{\ell 2}) \geq \dots \geq I(x, z_\ell) \quad (2)$$

implying that $I(x, z)$ decreases with depth, corresponding to increased $H(x|z)$ and reduced $H(z)$, which hinders MIA success [22].

However, the rate at which $I(x, z)$ decreases depends strongly on the network architecture and the representational capacity of each layer. In shallow or intermediate layers, high mutual information persists, leaving them vulnerable to inversion.

So, we challenge the common belief that deeper models are inherently more resistant to inversion attacks. As shown in Figure 2, even attacking the 6th (final) layer of a 6-layer Vision Transformer (ViT) [10] yields accurate reconstructions. Each layer retains a hybrid representation (1D decision token + 256D patch embeddings), producing a high-dimensional output of shape (257, 128) rich in instance-specific information. Despite the increased depth, the high-dimensional structure preserves the upper bound of $H(z)$, limiting the reduction in mutual information $I(x; z)$. According to Equation 1, the impact on $I(x; z)$ and the conditional entropy $H(x|z)$ is therefore marginal, leading to weak resistance against model inversion attacks.

With a properly designed inversion model, we achieve high-fidelity reconstructions from the final layer—a result not reported in prior work [2]. The model architecture and training code are detailed in Appendix. This underscores our key insight: depth alone is insufficient; only a significant reduction in mutual information can ensure inversion resistance. If the model is partitioned at this point, the defense no longer requires complex mechanisms.

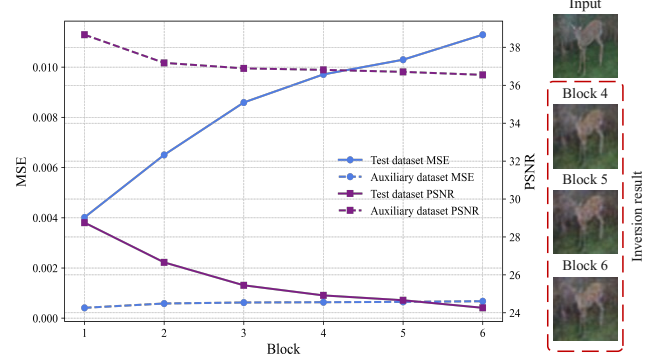


Figure 2: Comparison and visualization of mean squared error and peak signal-to-noise ratio after performing MIA on different depths of ViT (a total of 6 transformer blocks) (all settings are the same as in Section 4).

Definition 3.1 (Differential Entropy [28]). Let X be a continuous random vector in \mathbb{R}^d with probability density function $f_X(x)$. Its differential entropy is defined as

$$h(X) = - \int_{\mathbb{R}^d} f_X(x) \ln f_X(x) dx,$$

provided the integral exists.

LEMMA 3.2 (MAXIMUM ENTROPY PRINCIPLE FOR FIXED COVARIANCE [18]). Among all continuous distributions on \mathbb{R}^d with a given covariance matrix Σ , the Gaussian distribution $\mathcal{N}(\mu, \Sigma)$ uniquely maximizes the differential entropy. In particular, for any X with $\text{Cov}(X) = \Sigma$,

$$h(X) \leq h(\mathcal{N}(\mu, \Sigma)) = \frac{1}{2} \ln[(2\pi e)^d \det \Sigma].$$

In the following analysis, we will make use of Definition 3.1 and Lemma 3.2 to derive upper bounds on the differential entropy of both feature-level and decision-level activations.

Non-generative neural networks consistently exhibit a clustering behavior whereby intermediate representations collapse into a “decision region” that predominantly encodes class information. If we let $Z_{\text{dec}} \in \mathbb{R}^D$ denote the random variable corresponding to these decision-level activations, then its overall entropy satisfies

$$\begin{aligned} h(Z_{\text{dec}}) &= h(Z_{\text{dec}} | Y) + I(Y; Z_{\text{dec}}) \leq h(Z_{\text{dec}} | Y) + H(Y) \\ &\leq \max_c h(Z_{\text{dec}} | Y = c) + H(Y) \leq \max_c h(Z_{\text{dec}} | Y = c) + \ln K \end{aligned}$$

Next, we turn to the feature-level representations. Let $Z_{\text{feat}} \in \mathbb{R}^d$ denote the continuous random vector of intermediate features at some layer. By Lemma 2.2, among all distributions on \mathbb{R}^d with covariance Σ_{feat} ,

$$h(Z_{\text{feat}}) \leq h(\mathcal{N}(\mu_{\text{feat}}, \Sigma_{\text{feat}})) = \frac{1}{2} \ln[(2\pi e)^d \det \Sigma_{\text{feat}}].$$

Moreover, if we let $\sigma_{\text{feat}}^2 = \frac{1}{d} \text{tr}(\Sigma_{\text{feat}})$, then by the determinant–trace inequality $\det \Sigma_{\text{feat}} \leq (\sigma_{\text{feat}}^2)^d$ it follows that

$$h(Z_{\text{feat}}) \leq \frac{d}{2} \ln(2\pi e \sigma_{\text{feat}}^2) = O(d \ln \sigma_{\text{feat}}^2). \quad (3)$$

Similarly, for the decision-level representation we approximate each class-conditional distribution

$$Z_{\text{dec}} | Y = c \sim \mathcal{N}(\mu_c, \Sigma_c),$$

By Lemma 2.2, and applying the orthogonal spectral decomposition of Σ_c together with the Arithmetic Mean – Geometric Mean Inequality (AM-GM) inequality [13], we obtain

$$h(Z_{\text{dec}} | Y = c) \leq \frac{1}{2} \ln[(2\pi e)^D \det \Sigma_c] \leq \frac{D}{2} \ln\left(2\pi e \frac{R_c^2}{D}\right) \quad (4)$$

where R_c^2 denote the within-class mean-squared radius, i.e., $R_c^2 = \text{tr}(\Sigma_c) = \frac{1}{N_c} \sum_{i: y_i=c} \|z_i - \mu_c\|^2$. Refer to Appendix A for the above calculation details.

Combining Eqs. 3 and 4 gives

$$\begin{aligned} \Delta h &\equiv h(Z_{\text{feat}}) - h(Z_{\text{dec}}) \\ &\leq \frac{d}{2} \ln \sigma_{\text{feat}}^2 - \frac{D}{2} \ln\left(\frac{R_c^2}{D}\right) + \frac{d-D}{2} \ln(2\pi e) - \ln K. \end{aligned}$$

Thus the gap depends on d , D , $\text{tr}(\Sigma_{\text{feat}})$, and R_c^2 . Typically $d \geq D$ (often only $1-4 \times$ larger), and $\sigma_{\text{feat}}^2 = \frac{1}{d} \text{tr}(\Sigma_{\text{feat}})$ contains both intra- and inter-class variance, whereas $R_c^2 = \text{tr}(\Sigma_c)$ reflects only the within-class spread of class c . Consequently the first two logarithmic terms and the positive constant $\frac{d-D}{2} \ln(2\pi e)$ together create a sizeable positive gap, while the $\ln K$ correction is too small to offset it.

Although our theoretical bounds are formulated for the *differential entropy* of continuous random vectors, the same phenomenon carries over to the *Shannon entropy* of the finite-precision tensors actually stored at run time. In practice, each activation vector Z is quantised to a discrete tensor z , and entropies are estimated over mini-batches. By the quantisation lemma of Cover–Thomas [7, Thm. 12.3], this discretisation changes the entropy only by an additive term that depends on the dimensionality and the quantisation step. Hence the population-level drop in entropy from Z_{feat} to Z_{dec} remains—indeed is slightly amplified—when measured on individual activations z . A complete derivation is provided in Appendix B.

Using the upper bounds in Eqs. 3 and 4 together with the information identity in Eq. 1, we can derive a lower bound on $H(x|z)$, which quantifies the residual uncertainty of x given z :

$$\begin{aligned} H(x | z) &= H(x) - I(x; z) \\ &\geq H(x) - H(z) \text{ (regardless of whether } F_{\text{edge}} \text{ is deterministic)} \\ &\geq \begin{cases} H(x) - \frac{d}{2} \ln(2\pi e \sigma_{\text{feat}}^2), & z \in Z_{\text{feat}}, \\ H(x) - \frac{D}{2} \ln\left(2\pi e \frac{R_c^2}{D}\right) - \ln K, & z \in Z_{\text{dec}}. \end{cases} \end{aligned} \quad (5)$$

Since $H(x)$ is a constant in Eq. 5, the lower bound on $H(x|z)$ is dominated by the term that is subtracted from it. When z is a *decision-level* representation, this subtracted term $\frac{D}{2} \ln(2\pi e R_c^2/D)$ is typically smaller than its feature-level counterpart, so the bound on $H(x|z)$ is larger, i.e. there is more residual uncertainty about the input. In the decision layer this bound depends only on the D and the R_c^2 . As D is architectural and therefore constant during training, the key quantity we can influence is R_c^2 . Accordingly, the next question we ask is: *how does R_c^2 evolve through training, and can we deliberately control it?*

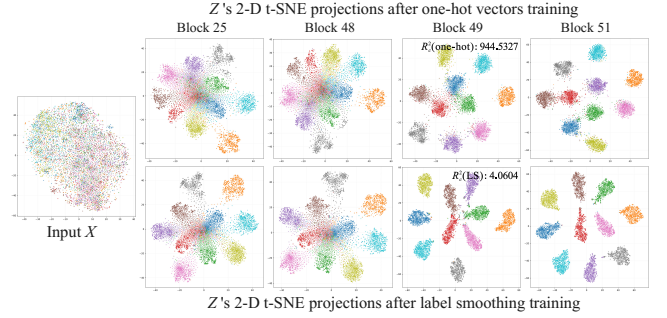


Figure 3: Layer-wise 2-D t-SNE of IR-152 features (all settings are the same as in Section 4).

3.2 Rethink Label Smoothing to MIA

With cross-entropy training and one-hot targets, the back propagated feature gradient is $\tilde{g}_i = J_i^\top \delta_i$ with $\delta_i = p_i - y_i$ (see Table 1). An SGD update $z_i^+ = z_i - \gamma \tilde{g}_i$ therefore induces the first-order change

$$\Delta R_c^2 = -\frac{2\gamma}{N_c} \sum_{i \in c} (z_i - \mu_c)^\top \tilde{g}_i \quad (6)$$

where the $1/N_c$ factor appears because R_c^2 is defined as a class average.

Substituting $\tilde{g}_i = J_i^\top (p_i - y_i)$ gives

$$\Delta R_c^2(\text{one-hot}) = -\frac{2\gamma}{N_c} \sum_{i \in c} \left[(p_{ic} - 1) T_{\text{corr},i} + \sum_{k \neq c} p_{ik} T_{k,i} \right] \quad (7)$$

where $T_{\text{corr},i} = (z_i - \mu_c)^\top J_i^\top e_c$ and $T_{k,i} = (z_i - \mu_c)^\top J_i^\top e_k$. (The full derivation is provided in Appendix C.)

Rewrite $T_{\text{corr},i}$ as $T_{\text{corr},i} = \|z_i - \mu_c\| \|J_i^\top e_c\| \cos \theta_i$, with θ_i the angle between $z_i - \mu_c$ and $J_i^\top e_c$. Empirically, $J_i^\top e_c$ points toward the direction that pulls a sample toward its class centre, so $0 \leq \theta_i < 90^\circ$ for nearly all training points; hence $T_{\text{corr},i} \geq 0$.

Because one-hot supervision ensures $p_{ic} \leq 1$, the factor $(p_{ic} - 1)$ satisfies $(p_{ic} - 1) \leq 0$. Therefore the product $(p_{ic} - 1) T_{\text{corr},i} \leq 0$, meaning the first term in Eq. 7 is non-positive for every sample.

The sign of the second (off-class) term in Eq. 7 may be positive or negative; in practice it is usually non-positive once the decision boundaries are shaped, but early in training some positive values can appear. During the *mid stage*, off-class probabilities p_{ik} are still moderate, yet their weighted contributions—dominated by non-positive or sign-mixed $T_{k,i}$ —cannot cancel the strictly negative first term $(p_{ic} - 1) T_{\text{corr},i}$. Hence the bracket in Eq. 7 remains negative, and the overall negative prefactor $-2\gamma/N_c$ makes $\Delta R_c^2(\text{one-hot}) > 0$, allowing the within-class radius to increase temporarily. As training proceeds, $p_{ic} \rightarrow 1$ and $p_{ik} \rightarrow 0$; both bracketed terms vanish, so $\Delta R_c^2(\text{one-hot}) \rightarrow 0$. The radius therefore stabilises, and via Eq. 5, the lower bound on $H(x | z)$ becomes essentially fixed.

Eq. 7 shows that the label format controls the scalar factors that multiply the terms $T_{\text{corr},i}$ and $T_{k,i}$. Under label smoothing (LS), the gradient becomes $\tilde{g}_i^{\text{LS}} = J_i^\top \tilde{\delta}_i$ with $\tilde{\delta}_i = p_i - y'_i$ (see Table 1). Replacing the one-hot coefficients $(p_{ic} - 1)$ and p_{ik} by their smoothed counterparts $(p_{ic} - 1 + \alpha)$ and $(p_{ik} - \alpha/K)$ yields

$$\Delta R_c^2(\text{LS}) = -\frac{2\gamma}{N_c} \sum_{i \in c} \left[(p_{ic} - 1 + \alpha) T_{\text{corr},i} + \sum_{k \neq c} (p_{ik} - \frac{\alpha}{K}) T_{k,i} \right]. \quad (8)$$

Setting $\alpha = 0$ recovers the one-hot result.

Under label smoothing, the target-class coefficient becomes $p_{ic} - 1 + \alpha \geq 0$ (typically $\alpha > 0$ in practice to improve generalisation) in the late stage, whereas each off-class coefficient $p_{ik} - \alpha/K$ is close to 0 and usually slightly negative because $p_{ik} \rightarrow 0$. Empirically, the positive contribution outweighs the small mixed-sign off-class sum, so the bracket in Eq. 8 is typically positive. With the overall prefactor, this makes $\Delta R_c^2(\text{LS}) < 0$ in most cases, implying a continued—though slower—contraction of the within-class mean-squared radius. Consequently, Eq. 5 indicates that $H(x|z)$ tends to increase, further reducing the information available to inversion attacks.

By analysing the network through the gradient norm lower bound, we find that one-hot supervision drives the feature-layer gradients to 0 at convergence, effectively freezing the shallow representations. In contrast, LS maintains a strictly positive lower bound on those gradients, so these layers continue to receive small but non-zero updates even in the late stage of training (see details in Appendix D). This sustained adjustment keeps early features more active and less redundant in channel, generally increases their entropy $H(z)$, and consequently makes them more susceptible to feature-level MIA attacks.

Figure 3 shows 2-D t-SNE [32] maps of IR-152 [15] features z after one-hot (top) and label-smoothed (bottom) training. Although t-SNE cannot quantify and reflect entropy or the class radius, it can illustrate that LS tightens class clusters earlier, and the decision layer is much more compact, hinting at a smaller within-class radius. We directly computed a batch of z 's R_c^2 at block 49 and found that the LS model yields a noticeably lower value.

Key Conclusion

In summary, training with label smoothing and partitioning the network at the decision-representation zone not only improves generalisation but also markedly strengthens resistance to MIA.

4 EXPERIMENTS

This section details the experimental setup and presents analysis from four perspectives: the effect of information representation on MIA, intermediate feature enhancement, inversion model enhancement, and the role of auxiliary versus target data types.

4.1 Experiment Setup

1) *Datasets*. All images used have a resolution of 64×64 . The datasets are described as follows, with data allocation detailed in Table 2:

- **CIFAR-10** [19]. A dataset containing 60,000 RGB images categorized into 10 classes.
- **FaceScrub** [25] & **CelebA** [24]. Two face-image datasets consisting of 100,000 images across 530 identities and 202,599 images spanning 10,177 celebrities, respectively. The dataset splitting procedure follows [36], with no overlap between identities in the two datasets.
- **MNIST** [20], **EMNIST** [5], & **KMNIST** [4]. Three grayscale handwritten character datasets: MNIST contains digits across 10 classes, EMNIST comprises 26 letter classes, and KMNIST includes 49 classes of Japanese cursive hiragana.

2) *Target Models*. To capture the representational transitions across various network depths, we selected three representative

Table 2: Dataset, model and intermediate-layer dimension information. + indicates positive factor training.

Data splits and auxiliary data		
Task	Train / Test	Auxiliary Data
CIFAR-10 (10 classes)	66.6% / 16.7%	16.7% of CIFAR-10
FaceScrub (530 classes)	80% / 20%	CelebA (non-individual overlapping)
KMNIST (49 classes)	70% / 15%	15% of KMNIST, MNIST, EMNIST
Model allocation and accuracy		
Task	Model	Accuracy
CIFAR-10	IR-152	One-hot: 90.59%, LS ⁺ : 90.76%, LS ⁻ : 90.49%
	VGG19	One-hot: 91.50%, LS ⁺ : 91.85%
	ViT (6-depth)	One-hot: 78.65%, LS ⁺ : 79.26%
FaceScrub	VGG19	LS ⁺ : 90.14%
KMNIST	VGG19	One-hot: 97.01%
Dimensions of information at different model depths		
Model	Block (Depth)	Dimensions
IR-152	3, 8; 25, 40, 48; 49, 50, 51	(64,32,32); (128,16,16); (256,8,8); (512,4,4)
VGG19	13; 17, 26; 30, 39; 43, 52	(128,32,32); (256,16,16); (512,8,8); (512,4,4)
ViT	1–6	(257,128)

deep visual models: IR-152 [15], a residual network known for mitigating gradient vanishing via skip connections, effectively preserving rich input details; VGG19 [30], a classical deep convolutional architecture characterized by purely sequential feature extraction without residual connections; and a Vision Transformer (ViT) [10], specifically employing a standard six-layer configuration (patch size 4, embedding 128, 10 attention heads), leveraging self-attention to capture global contextual features directly from image patches. Detailed model performance (accuracy) across different datasets and corresponding information dimensions at various network depths are presented in Table 2.

3) *Inversion Models*. Our inversion architecture follows the design principles of [36], with adaptive strengthening based on the depth and dimensionality of target features. When the spatial resolution drops to 4×4 , the combination of deep layers and Tanh activation leads to vanishing gradients; to mitigate this, we replace Tanh with PReLU [14]. Additionally, we incorporate decoupled enhancement strategies and an inversion-specific architectural redesign. Details are provided in Section 4.2, Part 3, and the full architecture is available at [URL].

4) *Implementation Details*. Target models are trained with Adam (learning rate $3e-4$, except VGG19 on FaceScrub, which uses SGD (learning rate 0.05)). Inversion models use Adam with $\beta_1 = 0.5$ and learning rate $2e-4$. All training employs ReduceLROnPlateau. Experiments are run on two RTX 4090 GPUs and an Intel Core i9-14900KF CPU (32 threads).

5) *Evaluation Metrics*. We use **mean squared error (MSE)** and **peak signal-to-noise ratio (PSNR)** for quantitative evaluation, and visual comparisons for qualitative analysis. Both MSE and PSNR are computed between reconstructed and original inputs; lower MSE and higher PSNR indicate better reconstruction quality, and thus weaker inversion resistance.

4.2 Experimental Results

1) *The effect of information representation on MIA*. As shown in Fig. 4, for IR-152, which employs residual skip connections, the forward

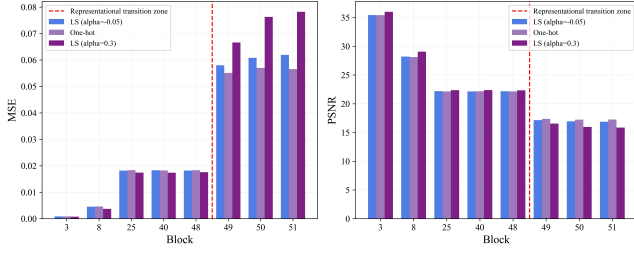


Figure 4: MIA performance results of different IR-152 layers.

Table 3: MIA performance on IR-152’s final outputs using different enhancement methods.

Position	Output Condition	Auxiliary Data Set		Test Data Set	
		MSE	PSNR	MSE	PSNR
Prediction	Normal	0.170175	12.509152	0.169263	12.510290
	LS ($\alpha = 0.3$)	0.165342	12.634348	0.163499	12.661634
	LS ($\alpha = -0.05$) [31]	0.171152	12.481016	0.169522	12.504991
	Log [36]	0.163476	12.685201	0.162863	12.676754
	Power (1/12) [39]	0.160062	12.757273	0.163184	12.667365

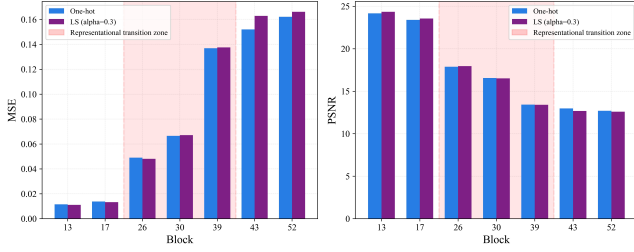


Figure 5: MIA performance results of different VGG19 layers.

accumulation of features slows down the transition of information representation. As a result, even up to the 48th block, the model maintains an MSE below 0.02—an empirical threshold indicating that high-fidelity reconstructions remain possible. However, once reaching Block 49, where the spatial resolution is reduced to 4×4 , the representation abruptly shifts to decision-level features, leading to a sharp rise in MSE.

Moreover, when trained with label smoothing (LS), the model shows a steady increase in MSE regardless of the sign of the smoothing factor α , while one-hot training keeps MSE relatively stable. PSNR follows a similar trend. LS with a positive α yields better resistance, consistent with the theory in Section 3. Struppek et al. [31] also observed that positive smoothing enhances MIA effectiveness in centralized settings—since LS increases prediction entropy, and by Eq. 1, higher entropy enables stronger MIA.

However, as discussed in the threat model (Section 2), CI inputs are privacy-sensitive. Table 3 compares different entropy-enhancing strategies. Although all three improve reconstruction quality (as noted in [31]), the resulting MSE exceeds 0.16—rendering the recovered inputs unlikely to pose a practical privacy threat.

As shown in Fig. 5, VGG19, lacking residual connections, exhibits a smoother transition in information representation. At Block 39,

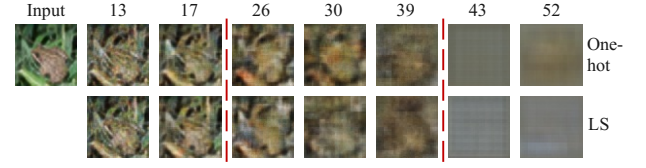


Figure 6: Visual performance of different VGG19 layers. Dotted lines distinguish the representational transition zone.

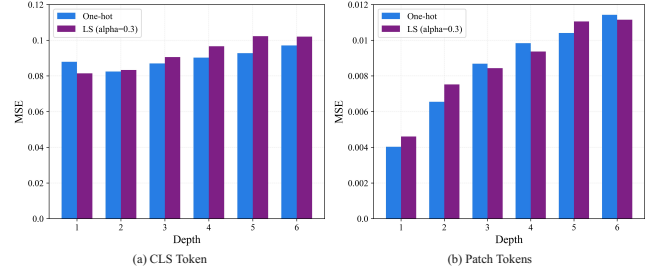


Figure 7: MIA performance results of different ViT layers.

the MSE rises sharply from 0.066493 at Block 30 to 0.136896, even though the spatial resolution remains at 8×8 , unlike IR-152. While prior studies often assume that decision-level information emerges in the final linear layers, our results suggest that, in models like VGG, this transition occurs much earlier, in the intermediate blocks. Compared to IR-152, VGG is therefore more suitable for lightweight edge-side partitioning in collaborative inference.

As further visualized in Fig. 6, reconstructions before Block 26 remain visually faithful, with MSE consistently below 0.02. Once the model enters the representational transition zone, reconstructions rapidly degrade, and when the features become purely decision-level, they lose semantic interpretability altogether.

Finally, as shown in Fig. 7, we perform reconstruction based on different partition points within ViT. When attacking using only the CLS token, the behavior under LS aligns with our theoretical analysis. However, when using patch tokens, the reconstruction quality exhibits noticeable fluctuations. This is attributed to the alternating influence of self-attention: one layer may pull representations toward the CLS token (favoring decision-oriented abstraction), while the next may refocus on patch-level features, resulting in the observed oscillation.

Notably, ViT’s output structure—consisting of a fixed number of 256 feature vectors—remains consistent across layers. This architectural design prevents the representational transition, meaning that no matter how deep the partition point is set, ViT fails to provide effective resistance against MIA.

2) *The effect of intermediate feature enhancement.* Prior work [22] has highlighted the critical role of feature entropy $H(z)$ in determining MIA susceptibility. To further assess the resistance of decision-representational regions, we design several enhancement strategies, summarized in Table 4, including an FFT-based method (Fast Fourier Transform[6]; global feature normalization via mean and variance, and neural network (NN)-based enhancement. Intermediate features are either residual-added to or concatenated with

Table 4: Attack results on Block-50 (decision-level) and Block-40 (feature-level) of IR-152 using different feature enhancement methods.

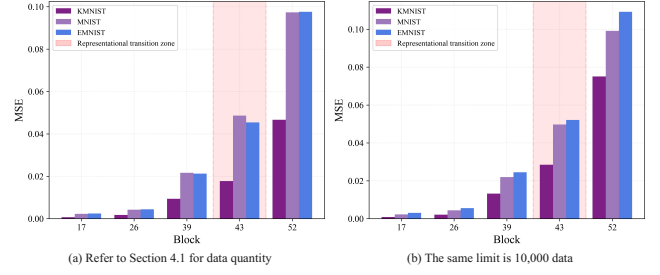
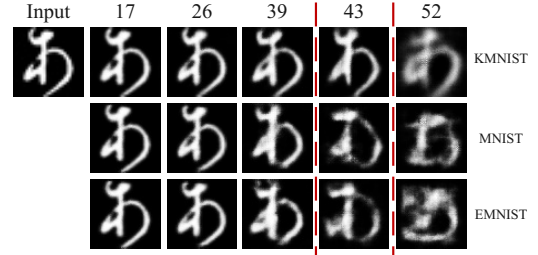
Method	Auxiliary Data Set		Test Data Set	
	MSE	PSNR	MSE	PSNR
Block-50-baseline	0.021366	21.500321	0.057010	17.224045
Augment by Analysis				
FFT (Residual)	0.089661	15.271254	0.112854	14.260188
FFT (Contact)	0.017355	22.411592	0.068011	16.458754
Normalize (Input)	0.022920	21.195560	0.056266	17.283856
Normalize (Residual)	0.022929	21.192309	0.056317	17.279251
Normalize (Contact)	0.023193	21.145331	0.055434	17.344250
Augment by NN				
w/o-Dropout (Residual)	0.014784	23.099889	0.061043	16.929223
with-Dropout (Residual)	0.016584	22.591667	0.055617	17.334325
w/o-Dropout (Contact)	0.018930	22.038503	0.057163	17.213750
with-Dropout (Contact)	0.016095	22.722609	0.051740	17.646756
Augment by Analysis & NN (Contact)				
Normalize (Input) & w/o-Dropout	0.015285	22.958731	0.055669	17.326721
Normalize (Input) & with-Dropout*	0.015489	22.891474	0.051937	17.627761
Block-40-baseline	0.011796	24.080942	0.018245	22.171516
Block-40-Augment*	0.004460	28.299952	0.014026	23.318254

Table 5: Attack results on Block-50 and Block-40 of IR-152 using different inversion model enhancement mechanisms.

Method	Auxiliary Data set		Test Data set	
	MSE	PSNR	MSE	PSNR
Block-50-baseline	0.021366	21.500321	0.057010	17.224045
MHA	0.018156	22.200025	0.052159	17.610650
AttentionAsConv	0.020217	21.736728	0.053299	17.515945
AttentionAsConv+SE	0.017121	22.458065	0.051737	17.647012
AttentionAsConv+SE+LSK+MSCA	0.019283	21.942643	0.050579	17.743654
Attention&Augment by NN with Dropout (Contact)*	0.013986	23.333684	0.049272	17.861294
Inversion-IR152	0.013218	23.589063	0.051795	17.643729
Block-40-baseline	0.011796	24.080942	0.018245	22.171516
Block-40-Augment*	0.003258	29.662543	0.011905	24.036657

their enhanced counterparts. Our experiments show that improper enhancement can cause the inversion model to overfit—achieving strong reconstruction on the auxiliary set while lacking generalization. NN-based methods without dropout are particularly prone to this. In contrast, combining global normalization with dropout-regularized NN modules effectively mitigates overfitting and improves attack quality. For example, PSNR gains on IR-152 reach only +0.4 at Block 50 but rise to around +1.13 at Block 40, indicating that enhancement strategies are more effective in the feature representation region, while decision-level layers remain robust against MIA.

3) *The effect of inversion model enhancement.* The design of the inversion model plays a critical role in capturing the true conditional entropy $H(x|z)$. Based on our existing architecture, we introduce attention mechanisms between deconvolutional blocks to improve representational capacity and mitigate overfitting. We first experimented with multi-head attention (MHA) [33], which led to performance gains but incurred nearly $10\times$ training cost. To balance efficiency and performance, we adopted the lightweight

**Figure 8: Reconstruction performance of KMIST data under different auxiliary data sets of VGG19.****Figure 9: Visual reconstruction performance of KMIST data under different auxiliary data sets of VGG19. Dotted lines distinguish the representational transition zone.**

Attention-as-Conv. To further enhance the model, we incrementally integrated this attention into shallow layers, augmented with Squeeze-and-Excitation (SE) modules [17]. In deeper blocks, we introduced large kernel attention (LSK) [26] and multi-scale channel attention (MSCA) [23] for stronger feature decoupling. Importantly, attention design in the inversion model should follow a weak-to-strong decoupling principle—light attention in early layers avoids overfitting, while deeper decoupled features help increase the expressiveness of $H(x|z)$. Our analysis confirms this intuition. Combined with feature enhancement, the improved model raises PSNR by +0.64 at Block 50 of IR-152. However, compared to the +1.9 gain in the feature representation region, this still reflects the inherently stronger MIA resistance of decision-level representations. Additionally, we explore a reverse-structured variant of the IR-152 residual block in the inversion model, which shows stronger expressiveness than basic deconvolutional stacks—though it still fails to achieve effective inversion in the decision region.

4) *The role of auxiliary versus target data types.* We conduct experiments using three grayscale datasets, targeting a handwritten Japanese character recognizer and using different auxiliary data types: KMIST (in-distribution), and MNIST and EMNIST (distributionally similar). As shown in Fig. 8, due to the simplicity of the input data, the representational transition zone is delayed. The presence of many zero-valued (black background) pixels in KMIST causes feature extraction to persist deeper into the network, with the transition zone occurring around Block 43. When training the inversion model with different auxiliary datasets, we observe

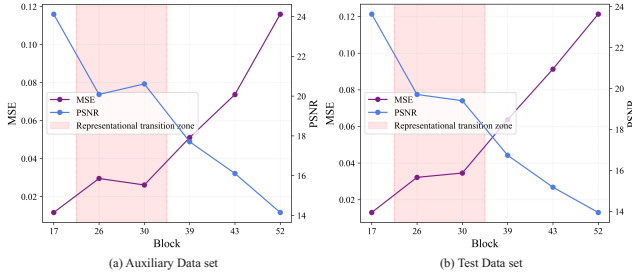


Figure 10: MIA performance across different layers of VGG19 trained with label smoothing on the FaceScrub dataset.



Figure 11: MIA visualization performance of different layers of VGG19 face recognizer after LS training. Dotted lines distinguish the representational transition zone.

that in-distribution data (KMNIST) yields significantly better reconstruction than similar but out-of-distribution datasets. Among the latter, performance improves with greater distributional proximity to the target. We also find that the larger sample size of EMNIST improves attack quality, but when sample sizes are equalized, MNIST performs better—suggesting it is closer in distribution to KMNIST. As visualized in Fig. 9, reconstructions before the transition zone are faithful across all auxiliary datasets, successfully recovering hiragana characters. However, after entering the transition or decision regions, the output drifts toward the auxiliary data distribution: MNIST-trained models tend to produce “0”-like digits, while EMNIST-trained models resemble characters like “D”.

We further investigate the case of face datasets, which exhibit low intra-class variation. As shown in Fig. 11, reconstructions ultimately converge to a representative frontal face for each class—resembling the behavior seen in Fig. 9. The consistency of samples within the 530 classes in FaceScrub causes the transition zone to shift earlier; MSE starts rising around Block 26 and climbs steeply after Block 30. Interestingly, although attacking CIFAR-10 used the same distribution, its large intra-class variance leads to poorer final reconstruction compared to both the structured handwriting datasets and the consistent face data. In such cases, reconstructions tend to regress toward the auxiliary data distribution only when the target representation has low variability.

5 RELATED WORK

Model inversion attacks in collaborative inference were first explored by He et al. [16], who demonstrated that shallow feature representations could be exploited to reconstruct input data. Subsequent research observed that increasing model depth helps resist

such attacks. Liu et al. [22] further clarified that the success of MIA is governed by information-theoretic factors such as mutual information and conditional entropy, etc.

During this period, advancements in attack methodology were relatively slow, as the original decoder architectures were already effective in reconstructing inputs from shallow features [36]. Notable developments include Yin et al. [37], who proposed a generative approach capable of performing attacks without auxiliary data, and Chen et al. [2], who introduced a diffusion-based method to approximate the inverse of forward models.

In contrast, defense strategies have seen more rapid innovation. Representative works include Wang et al. [34], who proposed deepening the model dynamically and adding differential privacy noise; Xia et al. [35] and Duan et al. [11], who introduced information-theoretic defenses by maximizing conditional entropy and estimating mutual information via CLUB (Contrastive Log Upper Bound), respectively; and Azizian et al. [1], who incorporated an autoencoder architecture to increase inversion resistance.

Across these defenses, two common patterns emerge: first, most approaches increase the model’s depth, which from our perspective accelerates the transition from feature to decision-level representations; second, they aim to increase $H(x|z)$ or reduce $H(z)$, in line with the theoretical framework introduced in [22]. However, these defenses typically incur accuracy degradation in the target model. Moreover, existing works continue to place the partition point in shallow layers, overlooking the importance of split location. The contribution of our work lies in identifying a theoretically optimal partition zone, enabling defenses to be more effective while reducing the impact on model accuracy.

6 DISCUSSION

Deployment Implications. Our results show that residual and Transformer-based models are less resistant to model inversion. Residual networks delay representation shifts, placing over 78% of parameters on the edge, while VGG-like models allow earlier partitioning with only 2.5% edge-side parameters, making them more suitable for collaborative inference. Transformers, due to persistent feature retention, are ill-suited for privacy-sensitive scenarios.

Auxiliary Data Assumptions. We conduct all CIFAR-10 experiments using same distribution data. While some defenses assume the adversary lacks such data, this is unrealistic in the era of big data. Assuming no prior knowledge is implausible and undermines the motivation for attack.

7 CONCLUSION

In this paper, we revisit model inversion threats in collaborative inference and demonstrate that increasing model depth does not necessarily resist MIA. Through theoretical analysis, we show that the representational transition zone induces a sharp rise in conditional entropy $H(x|z)$, with intra-class mean-squared radius R_c^2 and feature dimensionality D being the key factors influencing its lower bound. Our experiments on representative vision models reveal that partitioning at the decision-level representations yields an average $4\times$ increase in MSE compared to feature-level layers, and maintains a 66% advantage in resistance even when feature transmission and inversion models are both enhanced. Additionally, we find that

increasing the number of prediction classes shifts the transition boundary earlier, and data with greater intra-class variance offers stronger resistance against reconstruction.

REFERENCES

- [1] Bardia Azizian and Ivan V. Bajić. 2024. Privacy-Preserving Autoencoder for Collaborative Object Detection. *IEEE Transactions on Image Processing* 33 (2024), 4937–4951.
- [2] Dake Chen, Shiduo Li, Yuke Zhang, Chenghao Li, Souvik Kundu, and Peter A. Beereel. 2024. DIA: Diffusion based Inverse Network Attack on Collaborative Inference. In *Proceedings of the IEEE/CVF Conference on Computer Vision and Pattern Recognition*. 124–130.
- [3] Ting Chen, Simon Kornblith, Mohammad Norouzi, and Geoffrey Hinton. 2021. Attention as a convolutional layer. In *Proceedings of the IEEE/CVF International Conference on Computer Vision*. 979–988.
- [4] Tarin Clanuwat, Mikel Bober-Irizar, Asanobu Kitamoto, Alex Lamb, Kazuaki Yamamoto, and David Ha. 2018. Deep learning for classical japanese literature. *arXiv preprint arXiv:1812.01718* (2018).
- [5] Gregory Cohen, Saeed Afshar, Jonathan Tapson, and Andre Van Schaik. 2017. EMNIST: Extending MNIST to handwritten letters. In *2017 international joint conference on neural networks (IJCNN)*. IEEE, 2921–2926.
- [6] James W Cooley and John W Tukey. 1965. An algorithm for the machine calculation of complex Fourier series. *Mathematics of computation* 19, 90 (1965), 297–301.
- [7] Thomas M Cover and Joy A Thomas. 2006. *Elements of Information Theory*. John Wiley & Sons.
- [8] Tim Dierks and Eric Rescorla. 2008. *The transport layer security (TLS) protocol version 1.2*. Technical Report.
- [9] Shiwei Ding, Lan Zhang, Miao Pan, and Xiaoyong Yuan. 2024. PATROL: Privacy-oriented pruning for collaborative inference against model inversion attacks. In *Proceedings of the IEEE/CVF Winter Conference on Applications of Computer Vision*. 4716–4725.
- [10] Alexey Dosovitskiy, Lucas Beyer, Alexander Kolesnikov, Dirk Weissenborn, Xi-aohua Zhai, Thomas Unterthiner, Mostafa Dehghani, Matthias Minderer, Georg Heigold, Sylvain Gelly, et al. 2020. An image is worth 16x16 words: Transformers for image recognition at scale. *arXiv preprint arXiv:2010.11929* (2020).
- [11] Lin Duan, Jingwei Sun, and Yiran Chen. 2023. PrivaScissors: Enhance the Privacy of Collaborative Inference through the Lens of Mutual Information. *arXiv preprint arXiv:2306.07973* (2023).
- [12] Apple Security Engineering and Architecture. 2024. *Private Cloud Compute: A new frontier for AI privacy in the cloud*. Retrieved June 10, 2024 from <https://security.apple.com/blog/private-cloud-compute>
- [13] Godfrey Harold Hardy, John Edensor Littlewood, and George Pólya. 1952. *Inequalities*. Cambridge university press.
- [14] Kaiming He, Xiangyu Zhang, Shaoqing Ren, and Jian Sun. 2015. Delving deep into rectifiers: Surpassing human-level performance on imagenet classification. In *Proceedings of the IEEE international conference on computer vision*. 1026–1034.
- [15] Kaiming He, Xiangyu Zhang, Shaoqing Ren, and Jian Sun. 2016. Deep residual learning for image recognition. In *Proceedings of the IEEE conference on computer vision and pattern recognition*. 770–778.
- [16] Zecheng He, Tianwei Zhang, and Ruby B Lee. 2019. Model inversion attacks against collaborative inference. In *Proceedings of the 35th Annual Computer Security Applications Conference*. 148–162.
- [17] Jie Hu, Li Shen, and Gang Sun. 2018. Squeeze-and-excitation networks. In *Proceedings of the IEEE Conference on Computer Vision and Pattern Recognition*. 7132–7141.
- [18] Edwin T Jaynes. 1957. Information theory and statistical mechanics. *Physical review* 106, 4 (1957), 620.
- [19] Alex Krizhevsky and Geoffrey Hinton. 2009. Learning multiple layers of features from tiny images. 0 (2009).
- [20] Yann LeCun. 1998. The MNIST database of handwritten digits. <http://yann.lecun.com/exdb/mnist/> (1998).
- [21] Rongke Liu, Dong Wang, Yizhi Ren, Zhen Wang, Kaitian Guo, Qianqian Qin, and Xiaolei Liu. 2024. Unstoppable attack: Label-only model inversion via conditional diffusion model. *IEEE Transactions on Information Forensics and Security* (2024).
- [22] Rongke Liu, Youwen Zhu, Dong Wang, Gaoning Pan, Xingyu He, and Weizhi Meng. 2025. How Breakable Is Privacy: Probing and Resisting Model Inversion Attacks in Collaborative Inference. *arXiv e-prints*, Article arXiv:2501.00824 (Jan. 2025), arXiv:2501.00824 pages. arXiv:2501.00824 [cs.CR] doi:10.48550/arXiv.2501.00824
- [23] Ze Liu, Yutong Lin, Yue Cao, Han Hu, Yixuan Wei, Zheng Zhang, Stephen Lin, and Baining Guo. 2021. Swin transformer: Hierarchical vision transformer using shifted windows. In *Proceedings of the IEEE/CVF international conference on computer vision*. 10012–10022.
- [24] Ziwei Liu, Ping Luo, and Xiaogang Wang. 2015. Deep learning face attributes in the wild. In *Proceedings of the IEEE international conference on computer vision*. 3730–3738.
- [25] Hong-Wei Ng and Stefan Winkler. 2014. A data-driven approach to cleaning large face datasets. In *2014 IEEE international conference on image processing (ICIP)*. IEEE, 343–347.
- [26] Chao Peng, Xiangyu Zhang, Gang Yu, Guiming Luo, and Jian Sun. 2017. Large kernel matters—improve semantic segmentation by global convolutional network. In *Proceedings of the IEEE conference on computer vision and pattern recognition*. 4353–4361.
- [27] Yuben Qu, Hao Sun, and Chao Dong. 2024. Elastic Collaborative Edge Intelligence for UAV Swarm: Architecture, Challenges, and Opportunities. *IEEE Communications Magazine* 62, 1 (2024), 62–68.
- [28] Claude E Shannon. 1948. A mathematical theory of communication. *The Bell system technical journal* 27, 3 (1948), 379–423.
- [29] Nir Shlezinger and Ivan V Bajić. 2022. Collaborative inference for AI-empowered IoT devices. *IEEE Internet of Things Magazine* 5, 4 (2022), 92–98.
- [30] Karen Simonyan and Andrew Zisserman. 2014. Very deep convolutional networks for large-scale image recognition. *arXiv preprint arXiv:1409.1556* (2014).
- [31] Lukas Struppek, Dominik Hintersdorf, and Kristian Kersting. 2023. Be careful what you smooth for: Label smoothing can be a privacy shield but also a catalyst for model inversion attacks. *arXiv preprint arXiv:2310.06549* (2023).
- [32] Laurens Van der Maaten and Geoffrey Hinton. 2008. Visualizing data using t-SNE. *Journal of machine learning research* 9, 11 (2008).
- [33] Ashish Vaswani, Noam Shazeer, Niki Parmar, Jakob Uszkoreit, Llion Jones, Aidan N Gomez, Lukasz Kaiser, and Illia Polosukhin. 2017. Attention is all you need. In *Advances in Neural Information Processing Systems*. 5998–6008.
- [34] Yulong Wang, Xingshu Chen, and Qixu Wang. 2022. Privacy-preserving Security Inference Towards Cloud-Edge Collaborative Using Differential Privacy. *arXiv preprint arXiv:2212.06428* (2022).
- [35] Song Xia, Yi Yu, Wenhan Yang, Meiwen Ding, Zhuo Chen, Ling-Yu Duan, Alex C Kot, and Xudong Jiang. 2025. Theoretical Insights in Model Inversion Robustness and Conditional Entropy Maximization for Collaborative Inference Systems. In *Proceedings of the Computer Vision and Pattern Recognition Conference*. 8753–8763.
- [36] Ziqi Yang, Jiayi Zhang, and Ee-Chien Chang. 2019. Neural network inversion in adversarial setting via background knowledge alignment. In *Proceedings of the 2019 ACM SIGSAC Conference on Computer and Communications Security*. 225–240.
- [37] Yupeng Yin, Xianglong Zhang, Huanle Zhang, Feng Li, Yue Yu, Xiuzhen Cheng, and Pengfei Hu. 2023. Ginver: Generative model inversion attacks against collaborative inference. In *Proceedings of the ACM Web Conference 2023*. 2122–2131.
- [38] Yuheng Zhang, Ruoxi Jia, Hengzhi Pei, Wenxiao Wang, Bo Li, and Dawn Song. 2020. The secret revealer: Generative model-inversion attacks against deep neural networks. In *Proceedings of the IEEE/CVF conference on computer vision and pattern recognition*. 253–261.
- [39] Zeping Zhang, Xiaowen Wang, Jie Huang, and Shuaishuai Zhang. 2023. Analysis and utilization of hidden information in model inversion attacks. *IEEE Transactions on Information Forensics and Security* 18 (2023), 4449–4462.

A PROOF OF CLASS-CONDITIONAL ENTROPY UPPER BOUND

LEMMA A.1 (ENTROPY UPPER BOUND FOR CLASS-CONDITIONAL GAUSSIAN). *Let $Z_{\text{dec}} \in \mathbb{R}^D$ be the decision-level representation, and suppose that for each class $c \in \{1, \dots, K\}$, the conditional distribution satisfies*

$$Z_{\text{dec}} | Y = c \sim \mathcal{N}(\mu_c, \Sigma_c),$$

where Σ_c is the class-specific covariance matrix with spectral decomposition. Let $R_c^2 = \text{tr}(\Sigma_c)$ denote the class-wise mean-squared radius. Then the conditional entropy satisfies:

$$h(Z_{\text{dec}} | Y = c) \leq \frac{D}{2} \ln \left(2\pi e \cdot \frac{R_c^2}{D} \right).$$

PROOF. By the differential entropy formula for multivariate Gaussians,

$$h(Z_{\text{dec}} | Y = c) = \frac{1}{2} \ln \left[(2\pi e)^D \det \Sigma_c \right].$$

Let $\lambda_1, \dots, \lambda_D > 0$ be the eigenvalues of Σ_c . Then

$$\det \Sigma_c = \prod_{i=1}^D \lambda_i, \quad \text{tr}(\Sigma_c) = \sum_{i=1}^D \lambda_i = R_c^2.$$

Applying the arithmetic–geometric mean (AM–GM) inequality to the eigenvalues yields:

$$\prod_{i=1}^D \lambda_i \leq \left(\frac{1}{D} \sum_{i=1}^D \lambda_i \right)^D = \left(\frac{R_c^2}{D} \right)^D.$$

Substituting this into the entropy expression gives:

$$\begin{aligned} h(Z_{\text{dec}} | Y = c) &= \frac{1}{2} \ln \left[(2\pi e)^D \det \Sigma_c \right] \\ &\leq \frac{1}{2} \ln \left[(2\pi e)^D \cdot \left(\frac{R_c^2}{D} \right)^D \right] \\ &= \frac{D}{2} \ln \left(2\pi e \cdot \frac{R_c^2}{D} \right), \end{aligned}$$

□

B BATCH-LEVEL CONTRACTION CARRIES OVER TO INDIVIDUAL SAMPLES.

During training, the network processes a mini-batch $Z = (z^{(1)}, \dots, z^{(B)})$ of B i.i.d. samples, where each continuous vector $z^{(i)} \in \mathbb{R}^d$ (feature space) is mapped to $z_{\text{dec}}^{(i)} \in \mathbb{R}^D$ (decision space, $d \geq D$). Independence implies

$$h(Z_{\text{feat}}) = \sum_{i=1}^B h(z_{\text{feat}}^{(i)}), \quad h(Z_{\text{dec}}) = \sum_{i=1}^B h(z_{\text{dec}}^{(i)}).$$

Hence the proven batch-level inequality $h(Z_{\text{feat}}) > h(Z_{\text{dec}})$ already guarantees $h(z_{\text{feat}}^{(i)}) > h(z_{\text{dec}}^{(i)})$ for every sample i .

After uniform quantisation with step Δ , Cover–Thomas [7] yields

$$\begin{aligned} H(z_{\text{feat}, \Delta}^{(i)}) &= h(z_{\text{feat}}^{(i)}) + d \ln \frac{1}{\Delta} + o(1), \\ H(z_{\text{dec}, \Delta}^{(i)}) &= h(z_{\text{dec}}^{(i)}) + D \ln \frac{1}{\Delta} + o(1). \end{aligned}$$

Subtracting the two lines gives the per-sample Shannon-entropy gap

$$H(z_{\text{feat}, \Delta}^{(i)}) - H(z_{\text{dec}, \Delta}^{(i)}) = [h(z_{\text{feat}}^{(i)}) - h(z_{\text{dec}}^{(i)})] + (d - D) \ln \frac{1}{\Delta} + o(1).$$

Because $d \geq D$ and $\ln(1/\Delta) > 0$, the extra term $(d - D) \ln(1/\Delta)$ is non-negative. Thus the discrete entropy drop is at least as large as the differential-entropy drop, ensuring that the information contraction observed on the batch persists—indeed is slightly amplified—at the level of each individual finite-precision feature vector.

C R_c^2 UNDER ONE-HOT VECTORS

Consider a training sample i whose ground-truth class is c . Let

$$z_i \in \mathbb{R}^d, \quad \mu_c = \frac{1}{N_c} \sum_{i \in c} z_i, \quad R_c^2 = \frac{1}{N_c} \sum_{i \in c} \|z_i - \mu_c\|^2.$$

After one gradient step with learning rate γ ,

$$z_i^+ = z_i - \gamma \tilde{g}_i, \quad \mu_c^+ = \mu_c - \gamma \tilde{g}_c, \quad \tilde{g}_c = \frac{1}{N_c} \sum_{i \in c} \tilde{g}_i$$

With logits o_i and Jacobian $J_i = \partial o_i / \partial z_i$, the one-hot gradient is

$$\tilde{g}_i = J_i^\top (p_i - y_i) = (p_{ic} - 1) J_i^\top e_c + \sum_{k \neq c} p_{ik} J_i^\top e_k. \quad (\text{C.1})$$

We first write the updated radius in full:

$$R_c^{2+} := \frac{1}{N_c} \sum_{i \in c} \|z_i^+ - \mu_c^+\|^2.$$

Substituting the SGD updates $z_i^+ = z_i - \gamma \tilde{g}_i$ and $\mu_c^+ = \mu_c - \gamma \tilde{g}_c$,

$$\begin{aligned} R_c^{2+} &= \frac{1}{N_c} \sum_{i \in c} \|z_i - \gamma \tilde{g}_i - \mu_c + \gamma \tilde{g}_c\|^2 \\ &= \frac{1}{N_c} \sum_{i \in c} \|(z_i - \mu_c) - \gamma(\tilde{g}_i - \tilde{g}_c)\|^2. \end{aligned}$$

For any vectors a, b and scalar γ , $\|a - \gamma b\|^2 = \|a\|^2 - 2\gamma a^\top b + \gamma^2 \|b\|^2$. Applying this identity with $a = z_i - \mu_c$ and $b = \tilde{g}_i - \tilde{g}_c$,

$$\begin{aligned} R_c^{2+} &= \frac{1}{N_c} \sum_{i \in c} \left(\|z_i - \mu_c\|^2 - 2\gamma (z_i - \mu_c)^\top (\tilde{g}_i - \tilde{g}_c) + \gamma^2 \|\tilde{g}_i - \tilde{g}_c\|^2 \right) \\ &= R_c^2 - \frac{2\gamma}{N_c} \sum_{i \in c} (z_i - \mu_c)^\top (\tilde{g}_i - \tilde{g}_c) + \frac{\gamma^2}{N_c} \sum_{i \in c} \|\tilde{g}_i - \tilde{g}_c\|^2. \end{aligned}$$

Using $\sum_{i \in c} (z_i - \mu_c) = 0$, the increment can be written as a chain of equalities that shows each algebraic simplification explicitly:

$$\begin{aligned} \Delta R_c^2 &:= R_c^{2+} - R_c^2 \\ &= -\frac{2\gamma}{N_c} \sum_{i \in c} (z_i - \mu_c)^\top (\tilde{g}_i - \tilde{g}_c) + \frac{\gamma^2}{N_c} \sum_{i \in c} \|\tilde{g}_i - \tilde{g}_c\|^2 \\ &= -\frac{2\gamma}{N_c} \left[\sum_{i \in c} (z_i - \mu_c)^\top \tilde{g}_i - \left(\sum_{i \in c} (z_i - \mu_c) \right)^\top \tilde{g}_c \right] + O(\gamma^2) \\ &= -\frac{2\gamma}{N_c} \sum_{i \in c} (z_i - \mu_c)^\top \tilde{g}_i + O(\gamma^2). \end{aligned}$$

Therefore,

$$\Delta R_c^2 := -\frac{2\gamma}{N_c} \sum_{i \in c} (z_i - \mu_c)^\top \tilde{g}_i. \quad (\text{C.2})$$

Since we are interested only in the first-order effect and γ is sufficiently small, the $O(\gamma^2)$ term has been discarded.

Define

$$T_{\text{corr},i} := (z_i - \mu_c)^\top J_i^\top e_c, \quad T_{k,i} := (z_i - \mu_c)^\top J_i^\top e_k \quad (k \neq c).$$

Substituting (C.1) into (C.2) yields

$$\Delta R_c^2(\text{one-hot}) = -\frac{2\gamma}{N_c} \sum_{i \in c} \left[(p_{ic} - 1) T_{\text{corr},i} + \sum_{k \neq c} p_{ik} T_{k,i} \right].$$

D GRADIENT NORM LOWER BOUND UNDER LABEL SMOOTHING

Step 1: SVD inequality. Let J_ℓ be the Jacobian of the cloud-side sub-network at layer ℓ . Write its SVD $J_\ell = U \Sigma V^\top$ with $\Sigma = \text{diag}(\sigma_1, \dots, \sigma_r)$ and $\sigma_{\min}(J_\ell) = \sigma_r > 0$. For any vector $x \in \mathbb{R}^K$,

$$\|J_\ell^\top x\|_2 = \|\Sigma U^\top x\|_2 \geq \sigma_{\min}(J_\ell) \|x\|_2. \quad (\text{D.1})$$

Step 2: squared norms of the logit-level gradients. For a sample whose true class is c we define

$$\delta_i = p_i - y_i, \quad \tilde{\delta}_i = p_i - y'_i,$$

corresponding to one-hot and label-smoothed targets, respectively. Expanding every coordinate gives

$$\|\delta_i\|_2^2 = (p_{ic} - 1)^2 + \sum_{k \neq c} p_{ik}^2, \quad \|\tilde{\delta}_i\|_2^2 = (p_{ic} - 1 + \alpha)^2 + \sum_{k \neq c} \left(p_{ik} - \frac{\alpha}{K} \right)^2. \quad (\text{D.2})$$

At convergence $p_{ic} \rightarrow 1$ and $p_{ik} \rightarrow 0$ ($k \neq c$); substituting these limits into (D.2) yields

$$\|\delta_i\|_2^2 \rightarrow 0, \quad \|\tilde{\delta}_i\|_2^2 \rightarrow \alpha^2 + (K - 1) \left(\frac{\alpha}{K} \right)^2 =: c_\alpha^2 > 0. \quad (\text{D.3})$$

Step 3: lower bounds on feature-gradient norms. The feature-layer gradients are $g_{\ell,i} = J_\ell^\top \delta_i$ (one-hot) and $\tilde{g}_{\ell,i} = J_\ell^\top \tilde{\delta}_i$ (LS). Applying (D.1) to each error vector,

$$\|g_{\ell,i}\|_2 \geq \sigma_{\min}(J_\ell) \|\delta_i\|_2, \quad \|\tilde{g}_{\ell,i}\|_2 \geq \sigma_{\min}(J_\ell) \|\tilde{\delta}_i\|_2.$$

Combining with the limits in (D.3) we obtain

$$\|g_{\ell,i}\|_2^{\text{OH}} \rightarrow 0, \quad \|\tilde{g}_{\ell,i}\|_2^{\text{LS}} \geq \sigma_{\min}(J_\ell) c_\alpha > 0.$$

Thus, whereas one-hot cross-entropy drives the feature-layer gradients to vanish at convergence, label smoothing preserves a strictly positive lower bound proportional to $\sigma_{\min}(J_\ell) c_\alpha$.